

NeuroSwift: A Lightweight Cross-Subject Framework for fMRI Visual Reconstruction of Complex Scenes

Shiyi Zhang
Department of Biomedical
Engineering, Southern University of
Science and Technology
Shenzhen, China
sy.zhang4@siat.ac.cn

Dong Liang
Research Center for Medical AI,
Shenzhen Institutes of Advanced
Technology, Chinese Academy of
Sciences
Shenzhen, China
dong.liang@siat.ac.cn

Yihang Zhou*
Research Center for Medical AI,
Shenzhen Institutes of Advanced
Technology, Chinese Academy of
Sciences
Shenzhen, China
yh.zhou2@siat.ac.cn

Abstract

Reconstructing visual information from brain activity via computer vision technology provides an intuitive understanding of visual neural mechanisms. Despite progress in decoding fMRI data with generative models, achieving accurate cross-subject reconstruction of visual stimuli remains challenging and computationally demanding. This difficulty arises from inter-subject variability in neural representations and the brain's abstract encoding of core semantic features in complex visual inputs.

To address these challenges, we propose NeuroSwift, which integrates complementary adapters via diffusion: AutoKL for low-level features and CLIP for semantics. NeuroSwift's CLIP Adapter is trained on Stable Diffusion generated images paired with COCO captions to emulate higher visual cortex encoding. For cross-subject generalization, we pretrain on one subject then fine-tune only 17% parameters (FC layers) for new subjects, freezing other components. This enables state-of-the-art performance with only 1-hour training per subject on lightweight GPUs (three RTX4090), outperforming existing methods.

CCS Concepts

• **Human-centered computing** → **Human computer interaction (HCI)**; • **Computing methodologies** → **Artificial intelligence**.

Keywords

fMRI Visual Reconstruction, Brain-computer Interface, CLIP Guided Diffusion, Multi-Modal Fusion

1 Introduction

Human brain processes complex visual information efficiently, establishing multi-level neural representations [1–4]. Early approaches used VAEs or GANs for image synthesis [5–10] but lacked semantic accuracy. Following the NSD dataset [11], Takagi et al. [12] pioneered high-resolution reconstructions using diffusion models. Subsequent works [13–15] and recent models [16–19] employed conditional diffusion and cross-subject decoding to enhance semantic integration and generalizability.

*Corresponding Author

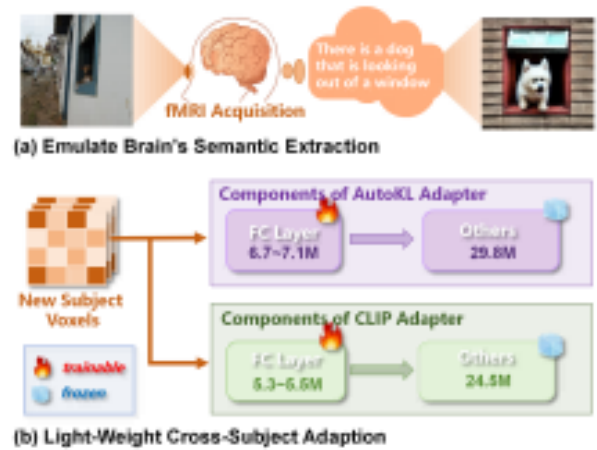


Figure 1: (a) During scanning, subjects imagine semantic content rather than raw visual stimuli. Therefore, we leverage COCO Captions to emulate imagined semantics and Semantic Images to emulate imagined scenes. (b) Efficient cross-subject adaptation. Pretrain on the first subject, then fine-tune only 17% of parameters on the other subjects in one hour with 3×RTX4090 GPUs.

However, existing methods generally suffer from two limitations. First, although models such as MindEye2[16] (64.4M parameters) and MindTuner[17] (76.6M parameters) have achieved cross-subject decoding capabilities, they demand high computational resources. For example, training MindEye2 requires eight NVIDIA A100 GPUs. Nevertheless, MindEye2's reconstruction performance in cross-subject generalization still falls short of the results it achieves when trained individually on each subject. Second, in complex visual scenes involving cluttered backgrounds, occlusions, small objects, and dense spatial structures, existing methods often struggle to reconstruct low-level details accurately while also capturing high-level semantic information.

To mitigate limitations in complex visual scenes, our framework employs COCO captions to guide semantic extraction: text embeddings are generated by a frozen Text Clipper, while image embeddings are obtained by synthesizing semantic images via Stable Diffusion followed by feature extraction with a frozen Image Clipper. For cross-subject generalization, we pretrain on Subj01 then fine-tune only the fully connected layers (17% of parameters)

in adapters for other subjects (Subj02/05/07), freezing other components. This reduces computational costs, requiring just three NVIDIA RTX4090 GPUs. With only one hour of training data, our method surpasses existing approaches, achieving efficient state-of-the-art cross-subject visual decoding under limited resources. Our contributions are summarized as follows:

- We propose a biologically inspired CLIP Adapter training mechanism that jointly processes synthetically generated semantic images and textual captions to emulate the brain's efficient semantic extraction.
- We introduce a cross-subject adaptation strategy where only 17% of lightweight FC layers are fine-tuned for new subjects, freezing all other components. This approach achieves state-of-the-art generalization capability with minimal resources, reducing computational costs compared to existing methods.
- Considering neuroanatomical variability, we employ individualized brain region masks with manually delineated ROI boundaries rather than the standardized templates typically used in previous research. This enables precise brain decoding for specific subjects.

2 Related Work

2.1 Diffusion Models

Diffusion Models (DMs) [7, 14, 20–23] generate samples through iterative denoising. Latent Diffusion Models (LDMs) operate in compressed latent spaces to reduce computational costs, with Stable Diffusion (SD) [24] being a widely-adopted LDM that leverages large-scale image-text datasets [25] to achieve superior text-to-image performance [8, 26, 27]. We employ SD to transform captions into semantic images. For final reconstruction, we use Versatile Diffusion (VD) [28] which employs a dual-guidance mechanism fusing CLIP features during denoising, trained on Laion2B-en [29] and COYO-700M [30], selected for its ability to integrate multimodal embeddings.

2.2 fMRI Visual Reconstruction

Decoding visual stimuli from brain activity progressed from pre-deep learning methods using image features like multi-scale local image bases[31, 32] and Gabor filters[33] with linear mappings, though limited by fMRI's low signal-to-noise ratio and small datasets. Deep neural networks later modeled nonlinear relationships [34] through architectures including deep belief networks[35], VAEs[36], feedforward networks[37, 38], GANs[7, 39], and hybrid VAE/GANs[10]. While these improved pixel-level reconstruction, they lacked semantic content until CLIP integration: Lin et al.[5] aligned fMRI patterns with CLIP's latent space via contrastive-adversarial learning, subsequently using StyleGAN2 to enhance semantic accuracy.

Since Stable Diffusion's successful application in various generative tasks[20, 25, 32, 40–42], Takagi et al.[12] pioneered mapping fMRI signals to diffusion latent space and CLIP text embeddings to generate images, though reconstructions lacked sufficient semantic information and natural qualities. Later, MindEye[15], which optimized the semantic representations of fMRI features through contrastive learning, and MindDiffuser[23], which devised a two-stage diffusion process, addressed this issue.

Recent advances in cross-subject decoding include MindEye2[16] enabling cross-subject alignment, MindTuner[17] bridging semantic gaps via visual fingerprinting and fMRI-to-text alignment, and BrainGuard[18] supporting privacy-preserving collaborative decoding. However, these methods still struggle to balance low-level structural feature extraction with high-level semantic understanding, particularly in complex visual scenes under cross-subject generalization, while requiring substantial computational resources.

3 NeuroSwift

In this section, we propose a hierarchical model termed NeuroSwift for vision reconstruction, and its framework is shown in Figure 2. The **structural generation** pipeline converts voxels into the latent space of Versatile Diffusion, which function as the diffusion prior. The **semantic reinforcement** pipeline aligns voxels with CLIP's text and image embeddings, which serve as conditional guidance for the diffusion process. Finally, the **diffusion reconstruction** process synthesizes the final image by integrating the structural prior and CLIP embeddings.

3.1 Structural Generation

The AutoKL Adapter transforms fMRI voxels to the latent space z_{pred} , and the frozen pre-trained AutoKL Decoder decodes it into a predicted image. We call it "structural generation" because it captures fundamental spatial structures and color distributions that serve as a latent diffusion prior, but it lacks detailed semantic content. See Appendix C for details of the AutoKL Adapter components.

The AutoKL Adapter is trained by minimizing the mean squared error between the predicted latent variable z_{pred} and the ground-truth latent variable z_{gt} , which is encoded from the visual stimulus using the frozen AutoKL Encoder:

$$\mathcal{L}_{MSE} = \frac{1}{n} \sum_{i=1}^n (z_{pred}^{(i)} - z_{gt}^{(i)})^2 \quad (1)$$

where n is the batch size.

3.2 Semantic Reinforcement

We designed a CLIP Adapter to map fMRI voxels into CLIP image and text embeddings, implementing semantic reinforcement that captures core semantics rather than structural features to condition the denoising process. The CLIP Adapter aligns predicted text embeddings e_{txt_pred} with e_{txt_clip} , where the latter is decoded by a pre-trained Text Clipper from textual captions corresponding to visual stimuli. Simultaneously, it aligns predicted image embeddings e_{img_pred} with e_{img_clip} , which is decoded by the pre-trained Image Clipper from semantic images generated by Stable Diffusion using the corresponding textual captions.

We use semantic images instead of original visual stimuli for CLIP image alignment because complex natural scenes often contain irrelevant content that may interfere with semantic extraction. In contrast, semantic images generated from textual captions retain only core information, thus reinforcing effectiveness. See Appendix D for details of the CLIP Adapter components.

Training objectives. The CLIP Adapter framework employs two types of loss functions to optimize the mapping of CLIP image and text embeddings. Among them, the *SoftCLIP loss*[15, 43] has

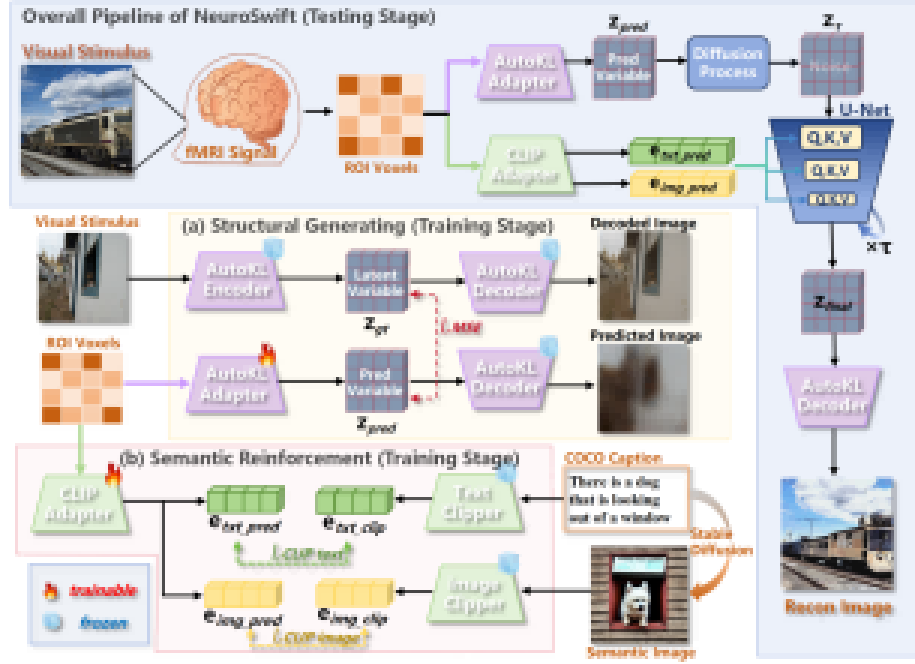


Figure 2: Overall structure of NeuroSwift in single-subject mode. fMRI voxels are processed through hierarchical pipelines: (a) The structural generation pipeline transforms voxels into latent space representations (z_{pred}), which serve as the diffusion prior for noise addition (z_τ). (b) The semantic reinforcement pipeline projects voxels into CLIP’s text (e_{txt_pred}) and image (e_{img_pred}) embeddings. Then, the denoising UNet iteratively refines the noise representation z_τ to integrate the CLIP semantic embeddings. Finally, the frozen AutoKL Decoder decodes z_{final} into the reconstructed image.

demonstrated effectiveness in aligning the fMRI modality with the pretrained CLIP embedding space. Within this framework, the loss function leverages a contrastive learning mechanism to maximize the similarity of positive pairs while minimizing the similarity of negative pairs.

$$\mathcal{L}_{SoftCLIP}(p, t) = - \sum_{i=1}^N \sum_{j=1}^N \left[\frac{\exp(t_i \cdot t_j / \tau)}{\sum_{m=1}^N \exp\left(\frac{t_i \cdot t_m}{\tau}\right)} \right] \times \log \left(\frac{\exp(p_i \cdot t_j / \tau)}{\sum_{m=1}^N \exp\left(\frac{p_i \cdot t_m}{\tau}\right)} \right) \quad (2)$$

Where p, t are the predicted CLIP embedding and target CLIP embedding in a batch of size N , respectively. τ is a temperature hyperparameter. However, using only the SoftCLIP loss causes noticeable artifacts because batch-wise soft labels create random variations, particularly with sparse and noisy fMRI-CLIP mappings. To address this, we introduced an MSE regularization term to ensure direct consistency between predicted and target CLIP embeddings. The complete set of losses for predicting image and text CLIP embeddings incorporating these two losses:

$$\mathcal{L}_{CLIPimage} = \mathcal{L}_{SoftCLIP}(e_{img_pred}, e_{img_clip}) + \mathcal{L}_{MSE}(e_{img_pred}, e_{img_clip}) \quad (3)$$

$$\mathcal{L}_{CLIPtext} = \mathcal{L}_{SoftCLIP}(e_{txt_pred}, e_{txt_clip}) + \mathcal{L}_{MSE}(e_{txt_pred}, e_{txt_clip}) \quad (4)$$

Here, e_{txt_clip} and e_{img_clip} represent the CLIP embeddings of text captions and their corresponding semantic images, where the captions are obtained using the COCO id of the visual stimuli, the semantic images are generated by Stable Diffusion using the captions.

3.3 Diffusion Reconstruction

The diffusion process synthesizes images that preserve structural features while maintaining semantic information.

Noise controlled initialization. The process initializes from the latent variable z_{pred} and adds partial noise controlled by the structural strength coefficient $s \in (0, 1]$. The initial noise step $\tau = N - \lfloor N \cdot s \rfloor$ (N is the total timesteps) determines the noise level for denoising. The noised latent z_τ is derived in one step:

$$z_\tau = \sqrt{\alpha_\tau} z_{pred} + \sqrt{1 - \alpha_\tau} \epsilon, \quad \epsilon \sim \mathcal{N}(0, I) \quad (5)$$

where α_τ is defined by the noise scheduler, ϵ is stochastic noise sampled from a standard normal distribution.

Semantic conditioning. The semantic constraints are imposed via cross-attention mechanisms, which guides the UNet during denoising. At each timestep τ_t , the UNet predicts noise:

$$\hat{\epsilon}_\theta(z_t, \tau_t, e_{input}) = \text{UNet}(z_t, \tau_t, \text{CrosAtt}(e_{txt_pred}, e_{img_pred})) \quad (6)$$

Guided denoising. The denoising process iteratively refines the latent vector z_τ through a sequence of timesteps $t \in [\tau, 0]$. At

each step t , the predicted noise $\hat{\epsilon}_\theta$ is used to update the latent state:

$$\mathbf{z}_{t-1} = \frac{1}{\sqrt{\alpha_t}} \left(\mathbf{z}_t - \frac{\beta_t}{\sqrt{1-\alpha_t}} \hat{\epsilon}_\theta(\mathbf{z}_t, t, \mathbf{e}_{input}) \right) + \sqrt{\beta_t} \cdot \epsilon \quad (7)$$

where β_t is defined by the noise scheduler, $\alpha_t = 1 - \beta_t$, $\bar{\alpha}_t$ is the cumulative product of signal retention coefficients. This update rule progressively removes noise while integrating semantic information guided by the multimodal condition \mathbf{e}_{input} .

Image reconstruction. Finally, \mathbf{z}_{final} is decoded into pixel space via the AutoKL Decoder \mathcal{D} , yielding the reconstructed image:

$$I_{recon} = \mathcal{D}(\mathbf{z}_{final}) \quad (8)$$

This diffusion process achieves structure-semantics decoupling: \mathbf{z}_{pred} provides blurred low-level visual primitives, while \mathbf{e}_{input} enforces high-level semantic concepts.

4 Results and Analyses

4.1 Data Elaboration

We utilize the Natural Scenes Dataset (NSD) [11], a 7T fMRI dataset of eight subjects viewing COCO images [44]. Following established methodologies [6, 12–15, 27], we analyze four subjects (Subj01, 02, 05, 07) with complete sessions. Our design includes: (a) 982-image shared test set; (b) subject-specific training/validation sets (8,859 images each). Preprocessed fMRI (1.8mm resolution) was masked using NSD-provided ROIs to extract ventral visual cortex voxels. The details of the data used in our experiments have been summarized in Appendix A.2.

Notably, previous studies have primarily relied on standardized brain templates for spatial parcellation. However, both neuroanatomical architecture and functional organization demonstrate significant inter-individual variability[45]. During spatial normalization, these inter-subject discrepancies can induce boundary blurring or registration inaccuracies, ultimately compromising model training efficacy and image reconstruction performance. In contrast to conventional approaches, our study utilizes NSD provided brain masks incorporating manually delineated ROI boundaries for individual subjects. These customized masks account for neuroanatomical and functional specificity through fine grained regional mapping, enabling differentiation of areas with subtle functional distinctions, thereby enhancing downstream processing precision.

4.2 Image Reconstruction Examples

To assess the effectiveness of our method in reconstructing semantic details and spatial structures in complex visual scenes, we followed the NeuroSwift implementation pipeline (Figure 2) and selected four stimuli with high semantic complexity for evaluation.

As shown in Figure 3, the figure consists of six columns: the first displays the original visual stimuli (ground truth), the second shows semantically refined images generated from COCO captions, the third presents reconstructions based on 40 hours of training data from Subj01, and the right three columns illustrate cross-subject generalization results, each obtained using only one hour of training data from three different subjects.

NeuroSwift effectively reconstructs the spatial layout and semantics of complex visual scenes. For example, in the final stimulus



Figure 3: Examples of NeuroSwift reconstructions from complex visual stimuli.

showing a small skier gliding through snowy pine woods, it accurately recovers key scene details via a hierarchical pipeline of spatial feature extraction and semantic enhancement.

Under cross-subject generalization, NeuroSwift also reconstructs complex images with high fidelity, including scenes such as “people dining,” “two boats,” and “a person cycling in a forest.” Notably, these results are achieved with training on just $3 \times \text{RTX4090}$ GPUs, highlighting its superior efficiency and generalization capability over existing methods.

4.3 Qualitative Comparison

In the qualitative experiments, we first compare the reconstruction results of NeuroSwift, fine-tuned with 1 hour of training data under the cross-subject generalization setting, against MindTuner[17] and MindEye2[16] under the same condition. We then compare our single-subject reconstruction results with those of MindBridge[43], trained with 40 hours of data under the single-subject setting.

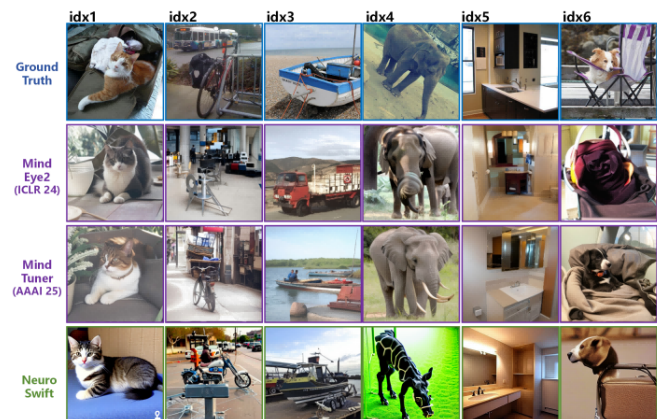


Figure 4: Comparison of our framework, MindEye2[16], and MindTuner[17] using 1h of training data in cross-subject adaptation mode.



Figure 5: Comparison of our framework with MindBridge[43] using 40h of training data in single-subject mode.

1-hour Data. Figure 4 shows that NeuroSwift outperforms both MindEye2 and MindTuner in cross-subject generalization on complex scenes. Take idx2, for example: the scene features a bicycle on a street. MindEye2 misses the bicycle entirely, and although MindTuner brings back the bicycle, it ignores the surrounding traffic. NeuroSwift, however, correctly reconstructs both the bicycle and the traffic flow. In idx3, which depicts a boat on a shore in the lower-right corner, MindEye2 mistakenly reconstructs a truck, and MindTuner places the boat out on the water. Only NeuroSwift accurately reproduces the boat sitting on the shore. These comparisons highlight NeuroSwift’s superior ability to restore spatial layout and semantic detail at the same time. However, occasional failures do occur. For instance, in idx4 (the “elephant” stimulus), neither MindEye2 nor NeuroSwift manages to recover the elephant.

40-hour Data. When reconstructing using 40 hours of data from a single subject, NeuroSwift outperforms MindBridge. In the six examples shown in Figure 5, both methods capture the core semantic content accurately, but MindBridge’s reconstructions exhibit spatial deviations from the original stimuli, whereas NeuroSwift achieves precise spatial recovery.

4.4 Quantitative Evaluation

To objectively measure reconstruction performance, we conduct quantitative evaluations benchmarking against four state-of-the-art approaches: MindEye2[16], MindBridge[43], MindTuner[17] and BrainGuard[18]. We assess low-level spatial coherence with SSIM [46] and pixel-wise accuracy via PixCorr [46], mid-level texture consistency using AlexNet(2/5) feature similarity [44], and high-level semantics with Incep [47], CLIP [48], EffNet-B [36], and SwAV [49]. Higher scores are better for SSIM, PixCorr, Alex(2), Alex(5), Incep and CLIP, while lower distances indicate superior performance for EffNet-B and SwAV.

1-hour Data. As Table 1 shows, with 1-hour of training data using only 3×RTX4090 GPUs under cross-subject setting, NeuroSwift demonstrates significant advantages. Its PixCorr (0.253) surpasses MindTuner (0.224) and MindEye2 (0.195) by 13% and 30% respectively, while SSIM (0.431) also leads competing methods. These results confirm its superior reconstruction of complex scenes, matching our qualitative observations of improved spatial structure recovery. For semantic understanding, NeuroSwift achieves highest in CLIP score (85.9%) and AlexNet(2) (90.7%), reflecting its exceptional semantic extraction capabilities.

Method	Pixcorr	SSIM	Alex(2)	Alex(5)	Incep	CLIP	EffNet-B↓	SwAV↓
MindEye2 (ICML 24)	.195	.419	84.2%	90.6%	81.2%	79.2%	.810	.468
MindTuner (AAAI 25)	<u>.224</u>	<u>.420</u>	87.8%	93.6%	84.8%	83.5%	.780	.440
NeuroSwift	.253	.431	90.7%	94.1%	88.6%	85.9%	<u>.791</u>	<u>.453</u>

Table 1: Quantitative comparison using 1h of training data under cross-subject mode. Bold indicates the best performance, while underline denotes the second-best.

The above results indicate that, despite its intermediate parameter count between MindEye2 (64.4M) and MindTuner (76.7M), NeuroSwift (66.3M) achieves more efficient cross-subject generalization via its dual-path architecture (AutoKL+CLIP) combined with subject-customized brain masks. This design avoids errors caused by imprecise registration inherent in standardized brain templates and enhances downstream processing precision through individualized ROI mapping to deliver cross-subject performance improvements.

Method	Pixcorr↑	SSIM↑	Alex(2)↑	Alex(5)↑	Incep↑	CLIP↑	EffNet-B↓	SwAV↓
MindBridge (CVPR 24)	.148	.259	86.9%	95.3%	92.2%	94.3%	.713	.413
MindEye2 (ICML 24)	<u>.322</u>	<u>.431</u>	96.1%	98.6%	95.4%	93.0%	.619	<u>.344</u>
MindTuner (AAAI 25)	<u>.322</u>	.421	95.8%	98.8%	95.6%	93.8%	.612	.340
BrainGuard (AAAI 25)	.313	.330	94.7%	97.8%	96.1%	96.4%	.624	.353
NeuroSwift	.335	.437	96.5%	98.1%	95.4%	97.1%	<u>.615</u>	<u>.354</u>

Table 2: Quantitative comparison using 40h of training data under single-subject mode.

40-hour Data. With 40 hours of training data in the single-subject mode, NeuroSwift also demonstrates performance improvements. As shown in Table 2, it achieves top-performing results in both PixCorr (0.335) and SSIM (0.437), supporting its superior spatial reconstruction capabilities observed in qualitative results. The remarkable breakthrough in CLIP score (97.1%) directly reflects its precise semantic content recovery (e.g., accurate reconstruction of bicycles and boats). Although EffNet-B (0.615) and SwAV (0.354) slightly underperform the optimal values.

4.5 Ablation studies

In ablation studies, we analyze NeuroSwift component contributions through modular removal in four configurations: “only z_{pred} ” retains solely the structural pipeline’s latent variable for Versatile Diffusion reconstruction without CLIP guidance; “w/o e_{txt_pred} ” removes text embedding guidance, reducing conditioning to image modality; “w/o e_{img_pred} ” disables image embedding guidance, using only text embeddings; “w/o z_{pred} ” disables the structural latent variable, initializing diffusion with $z_\tau = \epsilon \sim \mathcal{N}(0, \mathbf{I})$ and relying solely on text-image embeddings.

Qualitative results. As shown in Figure 6, the “only z_{pred} ” configuration preserves low-level spatial features (e.g., contours, layouts) but fails to generate identifiable semantic content due to the



Figure 6: Reconstruction examples from Subj01 with various ablations of the full model.

absence of CLIP embeddings. Conversely, the “w/o z_{pred} ” configuration captures primary semantic concepts but exhibits systematic deviations in spatial layouts without the structural prior constraint.

The “w/o e_{txt_pred} ” configuration maintains structural fidelity close to the full model through z_{pred} and e_{img_pred} synergy, but suffers semantic deterioration (e.g., scene/color inaccuracies), highlighting CLIP text embeddings’ role for abstract concepts. Meanwhile, the “w/o e_{img_pred} ” configuration accurately reconstructs semantics but shows reduced structural fidelity in some instances (e.g., object shapes), though z_{pred} maintains topological rationality.

Above results reveal that the structural prior ensures the fidelity of low-level spatial topology, CLIP text embeddings constrain abstract semantics, and CLIP image embeddings supplement fine-grained visual features.

Quantitative evaluation. As shown in Table 3, quantitative experiments demonstrate that when only the structural prior z_{pred} is retained (w/o e_{input}), spatial fidelity (SSIM=0.445) and texture consistency (AlexNet(2)=96.8%, AlexNet(5)=98.5%) are maximized, but all semantic metrics collapse (Inception=51.2%, CLIP=54.3%), confirming the qualitative observation of “clear contours but blurred semantics.” Conversely, removing z_{pred} (w/o z_{pred}) causes spatial structure to deteriorate dramatically (SSIM falls to 0.237), yet under CLIP’s multimodal guidance the semantic scores leap to the top (Inception=96.1%, CLIP=98.5%), corresponding to the qualitative case of “semantically accurate but misaligned layout.”

Furthermore, we analyzed the impact of neuroanatomical specificity by replacing manually customized mask with standardized brain template (std. template). While semantic metrics remained competitive, spatial and texture fidelity deteriorated: SSIM plunged

Method	Pixcorr \uparrow	SSIM \uparrow	Alex(2) \uparrow	Alex(5) \uparrow	Incep \uparrow	CLIP \uparrow	EffNet-B \downarrow	SwAV \downarrow
w/o e_{input}	.342	.374	95.1%	98.5%	51.2%	54.3%	.921	.958
w/o z_{pred}	.249	.237	74.1%	77.5%	95.3%	96.5%	.793	.402
NeuroSwift	.335	.437	96.5%	98.1%	95.4%	97.1%	.615	.354
std. template	.326	.357	94.8%	97.7%	94.9%	96.7%	.623	.355

Table 3: Quantitative comparison of the full model’s reconstruction results on Subj01 with its ablated configurations.

by 18.3% (0.357 vs. 0.437). This gap suggests that using conventional templates may induce boundary ambiguity during spatial normalization, thereby impairing low-level features (SSIM/AlexNet) while retaining only coarse semantic representations.

4.6 Interpretability of NeuroSwift

To investigate the importance of different brain regions in the NeuroSwift for visual reconstruction, we extracted the weight matrices of the AutoKL and CLIP Adapters’ fully connected layers and computed each voxel’s L2 norm as its activation contribution. Figure 7 shows the results obtained by training on 40 hours of data from Subj01 and fine-tuning with 1 hour of data from Subj02. The cross-subject fine-tuning results for Subj05 and Subj07 are provided in Appendix B.

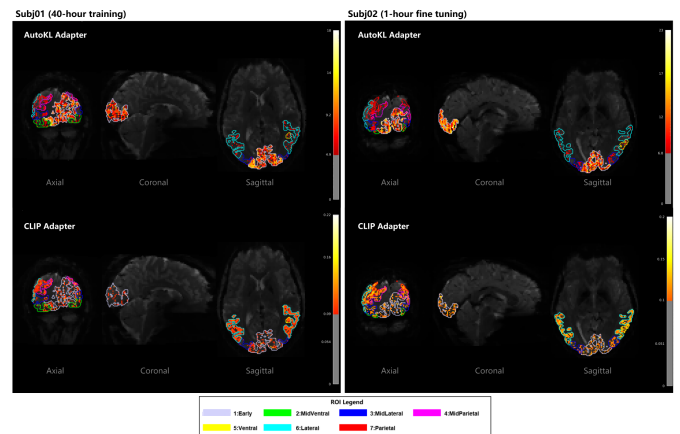


Figure 7: Spatial distribution of brain-region contributions in Subj01 for the AutoKL Adapter (a) and CLIP Adapter (b).

The AutoKL Adapter weight map shows prominent activation clusters in “Early” regions (V1-V3), indicating higher contributions to structural generation, consistent with its role in preserving low-level features like edges and textures. Conversely, it displays sparse activation in higher-order cortices (“Lateral”/“Parietal”). In contrast, the CLIP Adapter weight map exhibits continuous “lava flow” activation across “Ventral”, “Lateral”, and “Parietal” regions, paralleling its capacity to capture semantic information through multimodal integration. Conversely, sparse activations in primary/intermediate regions (Early, Midventral, etc.) indicate their limited semantic encoding contributions.

5 Conclusion and Limitations

NeuroSwift's dual-pathway architecture overcomes complex scene limitations: an AutoKL Adapter preserves low-level structural details while a biologically inspired CLIP Adapter extracts core semantics via synthetic images and text captions. Using manually delineated ROIs and pretraining with lightweight fine-tuning for new subjects, it achieves state-of-the-art cross-subject generalization with just one hour of data per subject on three RTX4090 GPUs.

Current limitations include dataset-specific validation, as significant differences in experimental design and signal acquisition restrict generalizability to the NSD dataset[11]. Future work will conduct cross-dataset validation on BOLD5000[50] to enhance robustness.

References

- [1] Bruno A Olshausen and David J Field. Emergence of simple-cell receptive field properties by learning a sparse code for natural images. *Nature*, 381(6583):607–609, 1996.
- [2] Rajesh PN Rao and Dana H Ballard. Predictive coding in the visual cortex: a functional interpretation of some extra-classical receptive-field effects. *Nature neuroscience*, 2(1):79–87, 1999.
- [3] William E Vinje and Jack L Gallant. Sparse coding and decorrelation in primary visual cortex during natural vision. *Science*, 287(5456):1273–1276, 2000.
- [4] Silvio Ionta. Visual neuropsychology in development: Anatomical-functional brain mechanisms of action/perception binding in health and disease. *Frontiers in Human Neuroscience*, 15:689912, 2021.
- [5] Sikun Lin, Thomas Sprague, and Ambuj K Singh. Mind reader: Reconstructing complex images from brain activities. *Advances in Neural Information Processing Systems*, 35:29624–29636, 2022.
- [6] Zijin Gu, Keith Jamison, Amy Kuceyeski, and Mert Sabuncu. Decoding natural image stimuli from fmri data with a surface-based convolutional network. *arXiv preprint arXiv:2212.02409*, 2022.
- [7] Katja Seeliger, Umut Güçlü, Luca Ambrogioni, Yagmur Güçlütürk, and Marcel AJ Van Gerven. Generative adversarial networks for reconstructing natural images from brain activity. *NeuroImage*, 181:775–785, 2018.
- [8] Milad Mozafari, Leila Reddy, and Rufin VanRullen. Reconstructing natural scenes from fmri patterns using bigbigan. In *2020 International joint conference on neural networks (IJCNN)*, pages 1–8. IEEE, 2020.
- [9] Tao Fang, Yu Qi, and Gang Pan. Reconstructing perceptive images from brain activity by shape-semantic gan. *Advances in Neural Information Processing Systems*, 33:13038–13048, 2020.
- [10] Ziqi Ren, Jie Li, Xuotong Xue, Xin Li, Fan Yang, Zhicheng Jiao, and Xinbo Gao. Reconstructing seen image from brain activity by visually-guided cognitive representation and adversarial learning. *NeuroImage*, 228:117602, 2021.
- [11] Emily J Allen, Ghislain St-Yves, Yihan Wu, Jesse L Breedlove, Jacob S Prince, Logan T Dowdle, Matthias Nau, Brad Caron, Franco Pestilli, Ian Charest, et al. A massive 7t fmri dataset to bridge cognitive neuroscience and artificial intelligence. *Nature neuroscience*, 25(1):116–126, 2022.
- [12] Yu Takagi and Shinji Nishimoto. High-resolution image reconstruction with latent diffusion models from human brain activity. In *Proceedings of the IEEE/CVF Conference on Computer Vision and Pattern Recognition*, pages 14453–14463, 2023.
- [13] Furkan Ozcelik and Rufin VanRullen. Natural scene reconstruction from fmri signals using generative latent diffusion. *Scientific Reports*, 13(1):15666, 2023.
- [14] Weijian Mai and Zhijun Zhang. Unibrain: Unify image reconstruction and captioning all in one diffusion model from human brain activity. *arXiv preprint arXiv:2308.07428*, 2023.
- [15] Paul Scotti, Atmadeep Banerjee, Jimmie Goode, Stepan Shabalin, Alex Nguyen, Aidan Dempster, Nathalie Verlinde, Elad Yundler, David Weisberg, Kenneth Norman, et al. Reconstructing the mind's eye: fmri-to-image with contrastive learning and diffusion priors. *Advances in Neural Information Processing Systems*, 36:24705–24728, 2023.
- [16] Paul S Scotti, Mihir Tripathy, Cesar Kadir Torrico Villanueva, Reese Kneeland, Tong Chen, Ashutosh Narang, Charan Santhirasegaran, Jonathan Xu, Thomas Naselaris, Kenneth A Norman, et al. Mindeye2: Shared-subject models enable fmri-to-image with 1 hour of data. *arXiv preprint arXiv:2403.11207*, 2024.
- [17] Zixuan Gong, Qi Zhang, Guangyin Bao, Lei Zhu, Rongtao Xu, Ke Liu, Liang Hu, and Duoqian Miao. Mindtuner: Cross-subject visual decoding with visual fingerprint and semantic correction. In *Proceedings of the AAAI Conference on Artificial Intelligence*, volume 39, pages 14247–14255, 2025.
- [18] Zhibo Tian, Ruijie Quan, Fan Ma, Kun Zhan, and Yi Yang. Brainguard: Privacy-preserving multisubject image reconstructions from brain activities. In *Proceedings of the AAAI Conference on Artificial Intelligence*, volume 39, pages 14414–14422, 2025.
- [19] Jingyang Huo, Yikai Wang, Yun Wang, Xuelin Qian, Chong Li, Yanwei Fu, and Jianfeng Feng. Neuropictor: Refining fmri-to-image reconstruction via multi-individual pretraining and multi-level modulation. In *European Conference on Computer Vision*, pages 56–73. Springer, 2024.
- [20] Prafulla Dhariwal and Alexander Nichol. Diffusion models beat gans on image synthesis. *Advances in neural information processing systems*, 34:8780–8794, 2021.
- [21] Chengbin Du, Yanxi Li, Zhongwei Qiu, and Chang Xu. Stable diffusion is unstable. *Advances in Neural Information Processing Systems*, 36:58648–58669, 2023.
- [22] Jonathan Ho, Ajay Jain, and Pieter Abbeel. Denoising diffusion probabilistic models. *Advances in neural information processing systems*, 33:6840–6851, 2020.
- [23] Yizhuo Lu, Changde Du, Qiongyi Zhou, Dianpeng Wang, and Huiguang He. Minddiffuser: Controlled image reconstruction from human brain activity with semantic and structural diffusion. In *Proceedings of the 31st ACM International Conference on Multimedia*, pages 5899–5908, 2023.
- [24] Robin Rombach, Andreas Blattmann, Dominik Lorenz, Patrick Esser, and Björn Ommer. High-resolution image synthesis with latent diffusion models. In *Proceedings of the IEEE/CVF conference on computer vision and pattern recognition*, pages 10684–10695, 2022.
- [25] Chitwan Saharia, William Chan, Saurabh Saxena, Lala Li, Jay Whang, Emily L Denton, Kamyar Ghasemipour, Raphael Gontijo Lopes, Burcu Karagol Ayan, Tim Salimans, et al. Photorealistic text-to-image diffusion models with deep language understanding. *Advances in neural information processing systems*, 35:36479–36494, 2022.
- [26] Jacob S Prince, Ian Charest, Jan W Kurzwski, John A Pyles, Michael J Tarr, and Kendrick N Kay. Improving the accuracy of single-trial fmri response estimates using glm-single. *Elife*, 11:e77599, 2022.
- [27] Weihao Xia, Raoul De Charette, Cengiz Oztireli, and Jing-Hao Xue. Dream: Visual decoding from reversing human visual system. In *Proceedings of the IEEE/CVF Winter Conference on Applications of Computer Vision*, pages 8226–8235, 2024.
- [28] Zhendong Wang, Yifan Jiang, Huangjie Zheng, Peihao Wang, Pengcheng He, Zhangyang Wang, Weizhu Chen, Mingyuan Zhou, et al. Patch diffusion: Faster and more data-efficient training of diffusion models. *Advances in neural information processing systems*, 36:72137–72154, 2023.
- [29] Christoph Schuhmann, Richard Vencu, Romain Beaumont, Robert Kaczmarczyk, Clayton Mullis, Aarush Katta, Theo Coombes, Jenia Jitsev, and Aran Komatsuzaki. Laion-400m: Open dataset of clip-filtered 400 million image-text pairs. *arXiv preprint arXiv:2111.02114*, 2021.
- [30] Minwoo Byeon, Beomhee Park, Haechon Kim, Sungjun Lee, Woonhyuk Baek, and Saehoon Kim. Coyo-700m: Image-text pair dataset, 2022.
- [31] Yoichi Miyawaki, Hajime Uchida, Okito Yamashita, Masa-aki Sato, Yusuke Morito, Hiroki C Tanabe, Norihiro Sadato, and Yukiyasu Kamitani. Visual image reconstruction from human brain activity using a combination of multiscale local image decoders. *Neuron*, 60(5):915–929, 2008.
- [32] Thomas Naselaris, Kendrick N Kay, Shinji Nishimoto, and Jack L Gallant. Encoding and decoding in fmri. *Neuroimage*, 56(2):400–410, 2011.
- [33] Takashi Yoshida and Kenichi Ohki. Natural images are reliably represented by sparse and variable populations of neurons in visual cortex. *Nature communications*, 11(1):872, 2020.
- [34] Tomoyasu Horikawa and Yukiyasu Kamitani. Generic decoding of seen and imagined objects using hierarchical visual features. *Nature communications*, 8(1):15037, 2017.
- [35] Marcel AJ Van Gerven, Floris P De Lange, and Tom Heskes. Neural decoding with hierarchical generative models. *Neural computation*, 22(12):3127–3142, 2010.
- [36] Rufin VanRullen and Leila Reddy. Reconstructing faces from fmri patterns using deep generative neural networks. *Communications biology*, 2(1):193, 2019.
- [37] Guohua Shen, Tomoyasu Horikawa, Kei Majima, and Yukiyasu Kamitani. Deep image reconstruction from human brain activity. *PLoS computational biology*, 15(1):e1006633, 2019.
- [38] Roman Bellis, Guy Gaziv, Assaf Hoogi, Francesca Strappini, Tal Golan, and Michal Irani. From voxels to pixels and back: Self-supervision in natural-image reconstruction from fmri. *Advances in Neural Information Processing Systems*, 32, 2019.
- [39] Ghislain St-Yves and Thomas Naselaris. Generative adversarial networks conditioned on brain activity reconstruct seen images. In *2018 IEEE international conference on systems, man, and cybernetics (SMC)*, pages 1054–1061. IEEE, 2018.
- [40] Chitwan Saharia, William Chan, Huiwen Chang, Chris Lee, Jonathan Ho, Tim Salimans, David Fleet, and Mohammad Norouzi. Palette: Image-to-image diffusion models. In *ACM SIGGRAPH 2022 conference proceedings*, pages 1–10, 2022.
- [41] Chitwan Saharia, Jonathan Ho, William Chan, Tim Salimans, David J Fleet, and Mohammad Norouzi. Image super-resolution via iterative refinement. *IEEE transactions on pattern analysis and machine intelligence*, 45(4):4713–4726, 2022.
- [42] Yulong Liu, Yongqiang Ma, Wei Zhou, Guibo Zhu, and Nanning Zheng. Brainclip: Bridging brain and visual-linguistic representation via clip for generic natural visual stimulus decoding. *arXiv preprint arXiv:2302.12971*, 2023.

- [43] Shizun Wang, Songhua Liu, Zhenxiong Tan, and Xinchao Wang. Mindbridge: A cross-subject brain decoding framework. In *Proceedings of the IEEE/CVF Conference on Computer Vision and Pattern Recognition*, pages 11333–11342, 2024.
- [44] Alex Krizhevsky, Ilya Sutskever, and Geoffrey E Hinton. Imagenet classification with deep convolutional neural networks. *Advances in neural information processing systems*, 25, 2012.
- [45] Marc M Himmelberg, Jonathan Winawer, and Marisa Carrasco. Linking individual differences in human primary visual cortex to contrast sensitivity around the visual field. *Nature communications*, 13(1):3309, 2022.
- [46] Zhou Wang, Alan C Bovik, Hamid R Sheikh, and Eero P Simoncelli. Image quality assessment: from error visibility to structural similarity. *IEEE transactions on image processing*, 13(4):600–612, 2004.
- [47] Christian Szegedy, Vincent Vanhoucke, Sergey Ioffe, Jon Shlens, and Zbigniew Wojna. Rethinking the inception architecture for computer vision. In *Proceedings of the IEEE conference on computer vision and pattern recognition*, pages 2818–2826, 2016.
- [48] Alec Radford, Jong Wook Kim, Chris Hallacy, Aditya Ramesh, Gabriel Goh, Sandhini Agarwal, Girish Sastry, Amanda Askell, Pamela Mishkin, Jack Clark, et al. Learning transferable visual models from natural language supervision. In *International conference on machine learning*, pages 8748–8763. PmlR, 2021.
- [49] Mathilde Caron, Ishan Misra, Julien Mairal, Priya Goyal, Piotr Bojanowski, and Armand Joulin. Unsupervised learning of visual features by contrasting cluster assignments. *Advances in neural information processing systems*, 33:9912–9924, 2020.
- [50] Nadine Chang, John A Pyles, Alex Marcus, Aditi Gupta, Michael J Tarr, and Elissa M Aminoff. Bold5000, a public fmri dataset while viewing 5000 visual images. *Scientific Data*, 6(1):49, 2019.

A Visual mechanisms and ROI selection

A.1 Visual neural mechanism

Our hierarchical visual reconstruction framework inspired by the brain’s multi-level visual processing mechanism. The process of turning light into vision begins in the eye. Light enters through the cornea and projects the retina, where photoreceptors convert it into neural signals. These signals are transported via the optic nerves to subcortical areas in the thalamus, such as the lateral geniculate and pulvinar nuclei, which then send the information mainly to the occipital lobe in the back of the brain. The occipital lobe is divided into several regions, including the primary visual cortex (V1) and interconnected higher-order visual areas. Therefore, we selected these regions as ROIs (see Figure 8).

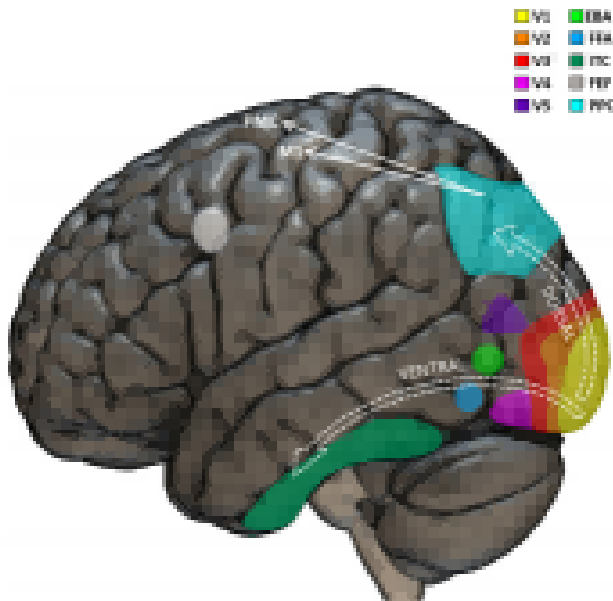


Figure 8: Graphical representation of the main cortical regions involved in visual perception. The image is cited from Lonta[4].

A.2 Functions of selected ROIs

We selected several regions of interest (ROIs) to capture key stages of visual processing. Table 4 outlines their principal functions and anatomical locations, which we describe in more detail below.

The **Early** visual cortices in the occipital lobe (V1, V2, V3) are responsible for processing low-level visual features such as edges, orientation, and contrast. The **MidVentral** area V4 primarily handles color and shape integration, while the **MidLateral** region V5/MT specializes in motion perception, encoding speed and direction. Additionally, the posterior parietal cortex (PPC), the **MidParietal** lobe, plays a crucial role in spatial attention, visuospatial positioning, and integrating multimodal visual information.

Further along the visual pathways, high-level areas contribute to advanced perceptual functions. The inferior temporal cortex (ITC) and fusiform face area (FFA) in the **Ventral** stream are responsible for object and face recognition, respectively, supporting

high-level visual cognition. In the **Lateral** regions, the extrastriate body area (EBA) processes body shapes and biological motion, while the frontal eye fields (FEF) coordinate eye movements and visual attention, enabling integration between visual perception and motor control. In the **Parietal** region, the posterior parietal cortex (PPC) plays a key role in spatial attention and visuomotor integration. Together, these regions form a hierarchical network supporting the full spectrum of visual processing.

ROI	Function	Anatomical Regions
Early	basic visual feature processing	V1, V2, V3
MidVentral	color/shape integration	V4
MidLateral	motion signal processing	V5
MidParietal	spatial attention transition	PPC
Ventral	object/face recognition	FFA, ITC
Lateral	body perception/eye movement control	EBA, FEF
Parietal	visuomotor coordination	PPC

Table 4: Visual Pathway (ROIs) we used, their primary functions, and corresponding anatomical regions.

Training	Validation	Test(shared)	ROIs	Subject ID	Voxels
8000	859	982	Early	Subj01	27638
			Midventral	Subj02	25217
			Midlateral		
			Midparietal	Subj05	23327
			Ventral	Subj07	21756
			Lateral		
			Parietal		

Table 5: The details of the NSD data we used in our experiments.

B Interpretability analysis results on other subjects

Figure 9 shows the weight distribution maps of both the AutoKL Adapter and CLIP Adapter for Subj05 and Subj07 under the fine-tuning mode with 1 hour of training data. These maps exhibit activation patterns similar to those of Subj02. For the mapping of the AutoKL Adapter, pronounced activation clusters in “Early” regions were observed in both subjects, with stronger weight contributions compared to “Midventral”, “Midlateral”, and “Midparietal” regions, where activations remained relatively sparse. The mapping of the CLIP Adapter weights retained the continuous and extended activation pattern across “Ventral”, “Lateral”, and “Parietal” regions, consistent with their role in multimodal semantic integration. While “Early”, “Midventral”, “Midlateral”, and “Midparietal” regions showed relatively less involvement, echoing the functional dissociation observed in Subj01 and Subj02.

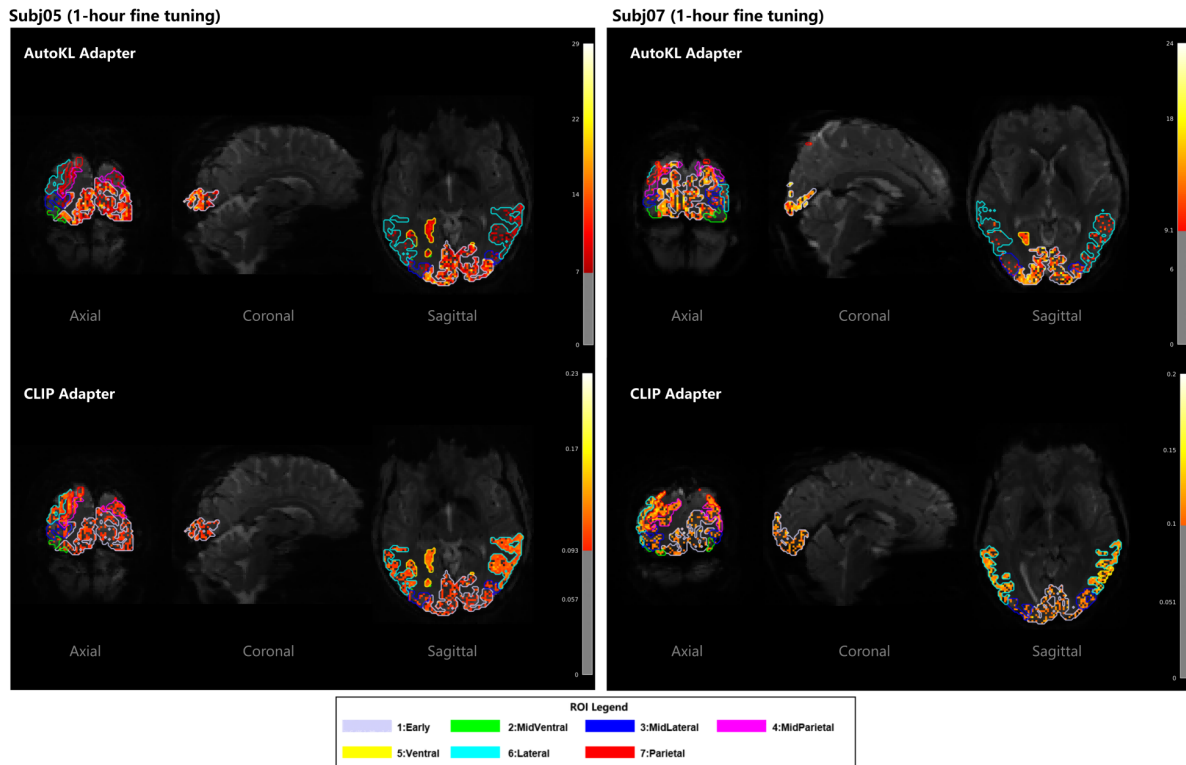


Figure 9: Spatial mapping of brain region contributions to AutoKL Adapter and CLIP Adapter on Subj05 and Subj07.

C Components of the AutoKL Adapter

The AutoKL Adapter first projects fMRI voxels into a hidden space via linear mapping, followed by sequential processing through LayerNorm, SiLU, and Dropout. These representations are then transformed by residual MLP blocks before being passed to a second linear layer that generates low-resolution feature maps. The maps undergo GroupNorm normalization and upsampling to produce the output z_{pred} , ensuring alignment with the latent vector z_{gt} , which is the variable encoded by the AutoKL Encoder from visual stimulus.

D Components of the CLIP Adapter

The CLIP Adapter framework uses an embedding network to compress inputs into a hidden space via linear projection, normalization, activation, and dropout, while a residual MLP refines features through cascaded blocks for stable gradients and semantic reinforcement. Subsequently separate linear heads project features into CLIP's multimodal spaces: the image head to e_{img_pred} (CLIP's image encoder) and the text head to e_{txt_pred} (CLIP's text encoder), maintaining distinct semantics while preserving CLIP's contrastive alignment. This architecture separates semantic enhancement and modality projection, maintaining compatibility with CLIP's pre-trained space while enabling authentic semantic information derived from brain signals.